AIAA JOURNAL
Vol. 30, No. 2, February 1992

Concentration Imaging Measurements in Turbulent Concentric-Jet Flows

M. Namazian* and J. Kelly†
Altex Technologies Corporation, Santa Clara, California 95054
and
R. W. Schefer‡
Sandia National Laboratories, Livermore, California 94550

Raman scattering images were used to determine the CH_4 concentration in nonreacting concentric-jet flows. The flow consists of a central CH_4 jet and a concentric air jet separated by a bluff body. Three jet velocity ratios were studied under isothermal conditions. At high momentum-flux ratios, the CH_4 jet penetrates the recirculation zone formed by the airflow behind the bluff body. At low momentum ratios, the jet is stagnated and fuel is dispersed into the recirculation zone. The large-scale instantaneous boundary between the stagnated jet and the air is time varying and creates a sharp peak in the rms CH_4 fluctuations in the stagnation region. Two-point spatial correlations were obtained over the flowfield to quantify the scale of the structures in these flows. Based on the limited data presented, it was found that the CH_4 concentration field is similar for equal momentum-flux ratios. The CH_4 concentration in the recirculation zone has a maximum at a momentum-flux ratio of unity, corresponding to the nearly penetrated case. In the nonpenetrated case, mixing of the central jet with surrounding air is substantially enhanced. Under these conditions, a considerable portion of the flowfield is mixed to conditions where combustion could occur. This enhanced mixing explains why bluff-body flames are more stable than jet flames into still air.

Introduction

TURBULENT concentric jets, separated by a bluff body, are one of the simplest flows that have recirculation and are therefore important to our fundamental understanding of turbulence and mixing in elliptic flows. This geometry also forms the basis for a number of practical combusting flows, commonly referred to as centerbody or bluff-body stabilized flames. Bluff-body stabilized flames are characterized by high turbulence intensities and mixing rates and upstream recirculation of high-temperature combustion products, which improves flame stabilization and combustion.[1] In addition, because of their relevance to many practical combustion devices, there has been considerable interest in developing numerical models for these flows.[2-4]

Bluff-body flows without a central-fuel jet have been studied extensively.[1,5,6] However, there are only limited data on bluff-body flows with a central-fuel jet. Most of the data on bluff bodies with central jets are velocity data.[7-10] Only limited species concentration measurements have been reported by Kimoto et al.[11]

Because of the importance of bluff bodies in aeropropulsion systems, the Air Force Wright Aeronautical Laboratories/Aero Propulsion Laboratory initiated an experimental and analytical bluff-body combustor study in 1977. The combustor studied had a large ratio of bluff-body to fuel-jet diameter and was in a ducted burner.[12] In the initial Air Force work, conventional flame photography and combustion probes were used to map out the stability and efficiency of the burner and to observe flame shapes and sooting tendencies. This work showed that, dependent upon burner operating conditions, many different types of flames (short blue, long yellow, etc.) of varying efficiencies and stability could be produced. Flames were categorized as either being airflow or fuel-jet-flow dominated, depending on whether the airflow was high or low, respectively. The difference between the cases was speculated to be associated with whether the fuel jet penetrated (fuel-jet dominated), or stagnated and was turned back (air-jet dominated) by the recirculation zone located downstream of the bluff body. Subsequent velocity measurements were used to measure the mean locations of the fuel and air stagnation points and establish the variation in their location with changes in the operating conditions.[13] It was shown that the mean behavior of the flow could be reasonably predicted by time-averaged models.[2,3,9] However, these models failed to predict the fluctuating components of the velocity field.[2,9] This failure was attributed to the unsteady nature of the flow and the presence of the large-scale structure. The presence of large-scale structures were subsequently confirmed in two-dimensional Mie scattering experiments.[14]

As an extension of the Air Force work, Li and Tankin[15] recently used flow visualization to determine the effect of burner design and flow conditions on fuel-jet penetration at low Reynolds numbers. Analytical expressions were developed to correlate experimental data on fuel-jet penetration and recirculation-zone size with inlet flow parameters and geometry. The effects of combustion on flow structure and time-averaged flow features were also investigated.

Cinematography[16] and Mie-scattering photography[17] clearly demonstrate the presence of large-scale, time-varying structures in bluff-body stabilized flames. This characteristic makes the interpretation of point measurement results difficult. Therefore, in the present study, planar imaging techniques

Presented as Paper 89-0058 at the AIAA 27th Aerospace Sciences Meeting, Reno, NV, Jan. 9–12, 1989; received Nov. 29, 1989; revision received Dec. 3, 1990; accepted for publication Feb. 6, 1991.
Copyright © 1991 by the American Institute of Aeronautics and Astronautics, Inc. All rights reserved.

*Principle Scientist III, 650 Nutman Road, Suite 114. Member AIAA.
†Principle Scientist I, 650 Nutman Road, Suite 114. Member AIAA.
‡Research Scientist, Combustion Research Facility. Member AIAA.

were used to obtain information on the large-scale features of these flows.

In previous publications,[17,18] the authors presented data on both nonreacting and reacting bluff-body flows to describe the effects of combustion heat release on turbulence characteristics. In these studies, direct flame photography was used to study the effect of flow variables on global flame characteristics. Planar flow visualization, using Mie scattering from seed particles added to the fuel jet, was used to visualize the instantaneous flow structure and mean flow streamlines. Two-color laser Doppler velocimetry measurements were used to fully characterize the turbulence.[10] Raman scattering imaging from CH_4, the fuel, was used to determine how the turbulence disperses the fuel.[19] Finally, combined CH_4 Raman scattering and CH laser-induced fluorescence imaging (a flame tracer) was used to determine the relationship between fuel concentration and flame development.[20]

In these previous publications, only measurements at one jet-to-air velocity ratio were reported. Flow, mixing, and combustion conditions change considerably as the velocity ratio is varied.[17,21] In the present paper, the effect of velocity ratio on fuel mixing and CH_4 concentration distribution is reported. Results are presented for nonreacting flows to eliminate the effects of combustion heat release and fuel consumption. Instantaneous, time-averaged mean and fluctuating concentrations and spatial correlation data are reported. The time-resolved planar images reveal flow and mixing structure information that is lost when time-averaged and instantaneous point measurement techniques are used. The average statistical quantities are described in terms of instantaneous flow structures.

Experimental

A schematic of the axisymmetric bluff-body flow apparatus is shown in Fig. 1. Methane was supplied through a 5.4-mm-diam tube located in the center of the bluff body at a nominal velocity of 21 m/s, giving a Reynolds number of 7×10^3. Air was supplied through a coaxial jet surrounding the 50-mm bluff body. In the plenum chamber (not shown), the air passed through a honeycomb and two layers of mesh screens, which controlled turbulence intensity at the exit to less than 0.7%, as measured by hot-wire anemometry. The major test matrix consisted of measurements over a range of annular air velocities, listed in Table 1. The sixth column in this table is the square root of the momentum-flux (i.e., per unit area) ratio. This ratio is designated by MR and defined as $\rho_j U_j^2/\rho_a U_a^2$, where ρ is the density, U the velocity, and j and a refer to central-fuel and the concentric-air jets respectively. Evidence presented in the following sections indicates that MR is an important similarity parameter.

To examine the trend of the data, limited tests were performed keeping the air velocity fixed at 15 m/s and changing the fuel velocity, as shown in Table 2.

The two-camera imaging system has been described previously.[19,22] The concentration images were obtained by simultaneously collecting Raman-scattered light with two cameras oriented perpendicular to a thin sheet of laser light passed through the axis of the flow. The dynamic range of the data was enhanced over single camera systems by the use of two cameras. One camera was used to obtain data from the central region of the jet where the methane concentration is high. The second, more sensitive, camera was used to obtain data from the region adjacent to the main fuel jet where the methane concentration is low. The use of two cameras increased the dynamic range by a factor of 10, from about 20 for a single camera to 200 for the two-camera system, and allowed concentration measurements down to 0.005 mole fraction.

Figure 2 shows the two-camera imaging system. The Sandia DIANA facility flashlamp-pumped dye laser was used to produce a 1-J/pulse, 444-nm beam with 0.3-nm frequency width. The beam was focused into a sheet of light by a multipass cell, which is described elsewhere.[23] The scattered light from the sheet was collected by two identical 24-mm-focal-length f 1.4 camera lenses located on each side of the sheet. The light from each side of the sheet was passed through 10-nm bandwidth interference filters centered at 510 nm that transmitted only the Raman CH_4 signal to an image-intensifier tube. The output face of each tube was coupled to a vidicon detector via a fiber-optic coupler. The image intensifiers were ITT proximity focused F4107 and F4111 microchannel plate tubes. Both intensifiers were gated to stay on for 4 μs, encompassing the 1.8-μs duration of the laser pulse. An LSI 11/23 computer was used to control the experiment; trigger the laser, cameras, and image intensifiers; coordinate the camera

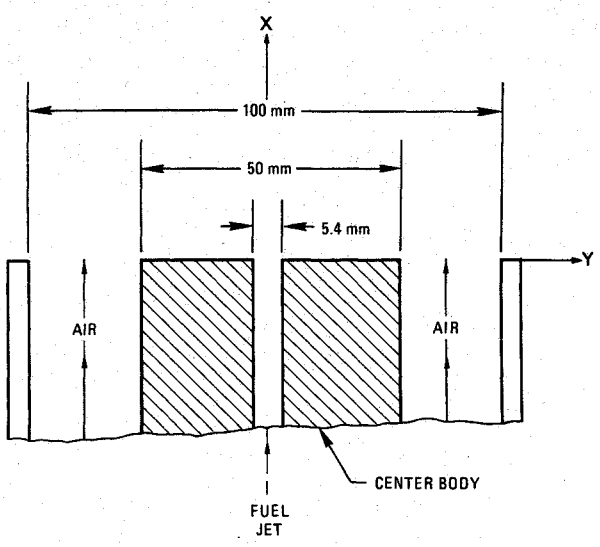

Fig. 1 Schematic of flow apparatus.

Table 2 Minor test matrix

Inner jet[a] velocity, u_j, m/s	Outer jet[b] velocity, u_a, m/s	u_j/u_a	Case
1.7	15	0.1	R
10.5	15	0.7	Q
21	15	1.4	M
42	15	2.8	P
77	15	5.1	O

[a]Methane. [b]Air.

Table 1 Major test matrix

Inner jet[a] velocity, u_j, m/s	Inner jet Reynolds no.	Outer jet[b] velocity, u_a, m/s	Outer jet Reynolds no.	u_j/u_a	$(u_j/u_a)\sqrt{\rho_j/\rho_a}$	Case
21	7000	0	0	∞	∞	D
21	7000	7.5	24,000	2.8	2.1	L
21	7000	15	48,000	1.4	1.0	M
21	7000	25	80,000	0.84	0.6	N

[a]Methane. [b]Air.

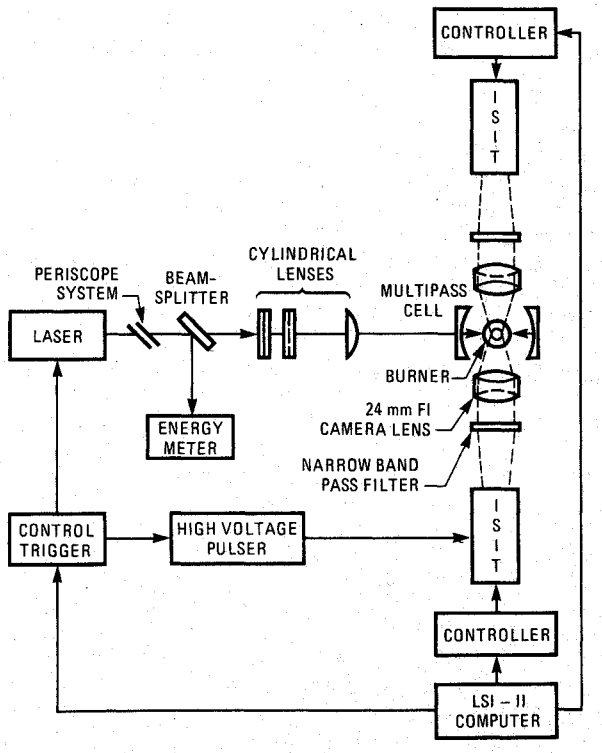

Fig. 2 Two-camera Raman imaging system.

scanning with the laser pulse; and store the data on a computer disk.

The camera equipped with the F4107 image intensifier was used to image the stronger of the central-fuel-jet region, and the camera equipped with the more intensified F4111 tube was used to record the weaker signal at the side of the fuel jet. The two cameras were aligned such that different, but overlapping, views were imaged by each camera. The areas imaged by the two detectors did not have identical scales because of differences in the magnification of the collection optics and detector heads. To ensure that the spatial relationship of the data from the two cameras was known, the image of a ruled target was recorded with both detectors. The target image data were then used to calculate the scaling and the translation factors that are required to properly join the data from the two detectors. With these scaling and translation factors, the original data were interpolated linearly so that each point in the overlapped region of the cameras corresponded to the same spatial location. The images were then joined at the midline of the overlapping region.

Both cameras were operated in a 100 × 100 pixel format with a field of view for each camera of about 40 (vertical) × 25 mm (horizontal). The images from the two cameras, when joined, covered a 40 × 40 mm total field of view. For each test condition of Table 1, 900 images were obtained over two ranges of axial distance. The first range corresponded to axial locations of 17–60 mm above the jet exit plane; the second corresponded to 55–98 mm above the burner face. For the test conditions of the minor matrix, Table 2, 200 images were obtained corresponding to axial locations of 22–60 mm.

The noise-related error in the concentration measurements was found by recording the signal from a dc-light-illuminated plane target and finding the standard deviation of the recorded signal. For example, to measure the noise in the more sensitive camera, the target was illuminated with a light-intensity level resulting in a recorded signal equivalent to 5% methane concentration. For this test, the same camera dial settings and filter arrangement were used as in the experiments. Two hundred images were obtained, and the standard deviation of the recorded signal was attributed to noise. The noise-to-signal ratio was found to be 3%. This test was repeated with a signal level equivalent to 20% methane concentration for the more sensitive camera, and with 50 and 100% for the other camera. In all cases, the noise-to-signal ratio was within 3%.

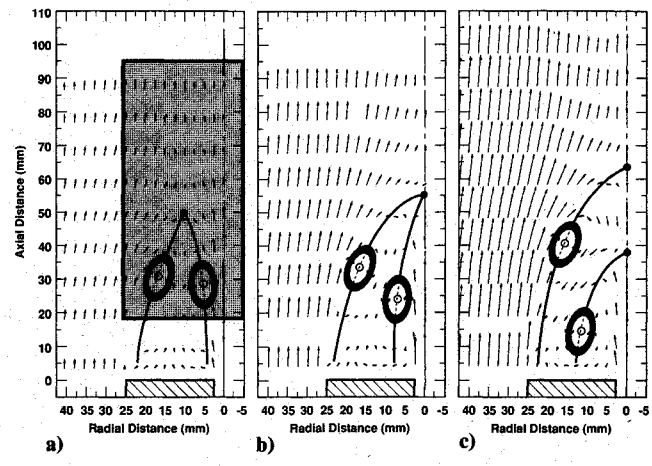

Fig. 3 Time-averaged velocity plots; imaging area is indicated by shaded region in case L, solid circles denote stagnation points, open circles denote centers of fuel- and air-driven vortices: a) case L; b) case M; c) case N.

The spatial resolution of the experiment is 0.4 × 0.4 × 0.3 mm, and a representative Kolmogorov length scale is around 0.16 mm. This value is calculated for case N at y = 12.5 mm and x = 40 mm using $\eta = L_I Re_t^{-3/4}$ where L_I is the integral length scale and Re_t is the turbulent Reynolds number, $Re_t = u'L_I/\nu$, with u' = 5 m/s and L_I = 25 mm; u' is a measured value reported previously[10] and L_I is assumed to be half the bluff-body diameter. Note that the methane Schmidt number is 0.80, which indicates that the scalar microscale length is close to the Kolmogorov length scale. Therefore, the experimental resolution of 0.4 mm is around twice the scalar microscale length.

The reproducibility of the data was established by comparing mean values obtained for the test conditions of major (Table 1) and minor (Table 2) test matrices. It was found that the mean and fluctuating (rms) results of these tests taken months apart are the same within 98 and 90% precision, respectively. Considering that only 200 images were obtained for the minor test matrix cases, this agreement is reasonable.

The concentration data to be presented, designated by C, are normalized by the methane number density for 100% methane at STP conditions. Results can be converted to number density by multiplying C by 2.5×10^{19} molecules/cm^3. For the isothermal conditions presented here, C is equivalent to CH_4 mole fraction.

Results

General Flowfield

Velocity measurements[10] have shown that the general flow pattern for bluff-body flows varies significantly with changes in the relative velocities of the central jet and annular air. Shown in Figs. 3 are the time-averaged velocity vector plots of the flowfield for the cases L, M, and N of Table 1. The measurements are shown on one side of the centerline, although data were taken on both sides to verify that the flow was symmetric. Superimposed on the velocity field (case L only) is the area imaged in the present measurements so as to better orient the reader to the location of concentration measurements presented later. The actual imaging area extends to approximately 15 mm on the opposite side of the centerline. In all cases, the annular air converges toward the centerline and forms a wake region that extends approximately one bluff-body diameter downstream of the bluff-body face. A toroidal recirculating-flow region is formed within the wake by the interaction of the annular air with the central

jet. Between the converging airflow and the central jet are two counter-rotating vortices, which are highlighted to indicate approximate location and direction of rotation. The first, an air-driven vortex located adjacent to the central jet, is driven by the shear layer that separates off the bluff-body corner. The second, a fuel-driven vortex located adjacent to the central jet, is generated by the shear layer that separates off the lip of the fuel tube.

Although the general flow features just described are present in all three flows, other features of the wake region vary significantly, depending on whether the flow is jet dominated (MR > 1) or air dominated (MR < 1). At high MR (case L in Fig. 3a), the central-jet dynamic pressure overcomes that of the air jet and the central jet penetrates through the recirculation zone formed behind the bluff body. Note that the axial velocity remains positive along the centerline and no on-axis stagnation points exist. As the MR is reduced (case M in Fig. 3b), the fuel jet and the recirculating air pressures become comparable (MR = 1) and the central jet is stagnated on the axis. Finally, in case N (Fig. 3c), the air dynamic pressure is dominant and two stagnation points form along the centerline. The upstream stagnation point (referred to as the fuel stagnation point) corresponds to the point where the fuel jet stagnates and is turned upstream and outward by the opposing reverse flow of the air. The downstream stagnation point corresponds to the end of the vortex region established by the inward flow of the annular air and is referred to as the air stagnation point. Note that, in case M, the fuel-jet stagnation point merges with the air stagnation point.

Further analysis of the velocity data clearly showed that the time-averaged interpretation of bluff-body flows is considerably different from the instantaneous behavior.[10] In particular, probability distributions of axial and radial velocity in the stagnation region are clearly bimodal, as is indicative of flows characterized by large-scale structure and intermittent mixing.[10] Velocity measurements conditional on the jet fluid and on the annular air show that the two modes of the bimodal distributions are associated with the alternate passage of large-scale structures consisting of either upstream-flowing air or downstream-moving jet fluid. The high velocity fluctuations measured in the stagnation region are directly attributable to this large-scale intermittency. Concentration data presented in the following sections confirm this conclusion.

Large-Scale Fluctuations

Axial and radial profiles of the time-averaged mean and fluctuating CH_4 concentration were obtained by averaging 900 instantaneous images at selected locations for the four velocity ratios of Table 1. Centerline profiles of the mean CH_4 concentration are shown in Fig. 4. Since the entering fuel and air densities remain constant, the velocity ratio is directly proportional to the square root of the momentum-flux ratio. The results show that, as the jet-to-air velocity ratio increases, the rate of decay in the axial concentration profile increases; i.e., mixing is enhanced. Figure 5 shows the corresponding concentration fluctuation (rms) profiles normalized by the mean centerline concentrations. In all cases the fluctuations depart from the corresponding values for a free jet (D case). In case L, the fluctuation profile increases monotonically over the field measured, and in cases M and N, the profiles reach a maximum value and then drop back to the free jet values.

To explain these observations, many instantaneous concentration images were analyzed. From these images, it was found that, in the low air-velocity case L (MR < 1), the central jet penetrates through the recirculation zone formed behind the bluff body. In the case M (MR ≈ 1), the central jet intermittently penetrates the recirculation zone. This behavior is clearly seen in numerous images, which show either a continuous central jet passing through the downstream end of the recirculation zone or a jet that is stagnated by upstream flowing air and dispersed into the recirculation zone. Finally, in case N (MR > 1), the central jet is always turned back upstream into the recirculation zone.[19]

Figure 6 shows a sample of the instantaneous CH_4 concentration centerline profiles for the three cases. In the nonpenetrating case (N in Fig. 6), a sharp drop in the instantaneous concentration is observed at $x \approx 40$ mm; this sharp drop defines the boundary between the stagnated fuel jet and the recirculating airflow. A similar drop in case M is observed at $x \approx 50$ mm. For both cases, the location of this boundary varies with time. In the penetrating case L (Fig. 6), no sharp drop is observed in the instantaneous concentration profile. The high concentration fluctuations for cases M and N shown

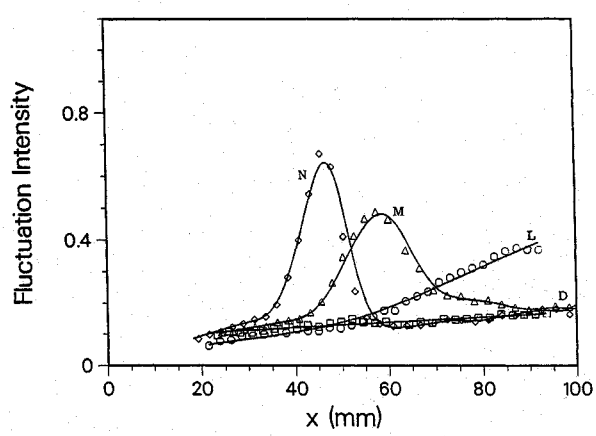

Fig. 5 Time-averaged centerline profiles of the fluctuating (rms) CH_4 concentration normalized by the mean CH_4 concentration.

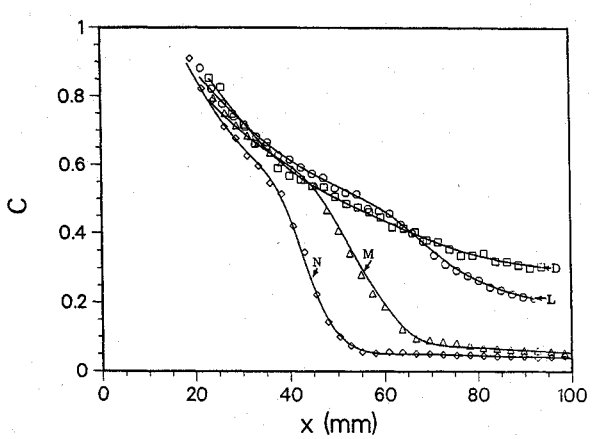

Fig. 4 Time-averaged centerline profiles of the mean CH_4 concentration.

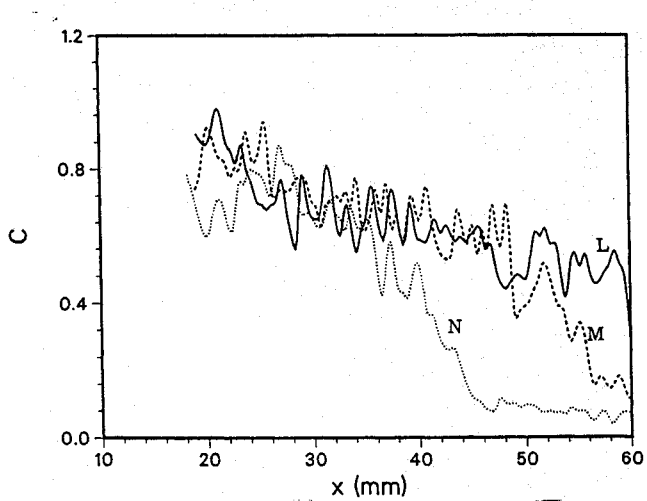

Fig. 6 Instantaneous centerline profiles of the CH_4 concentration: solid line, case L; dashed line, case M; dotted line, case N.

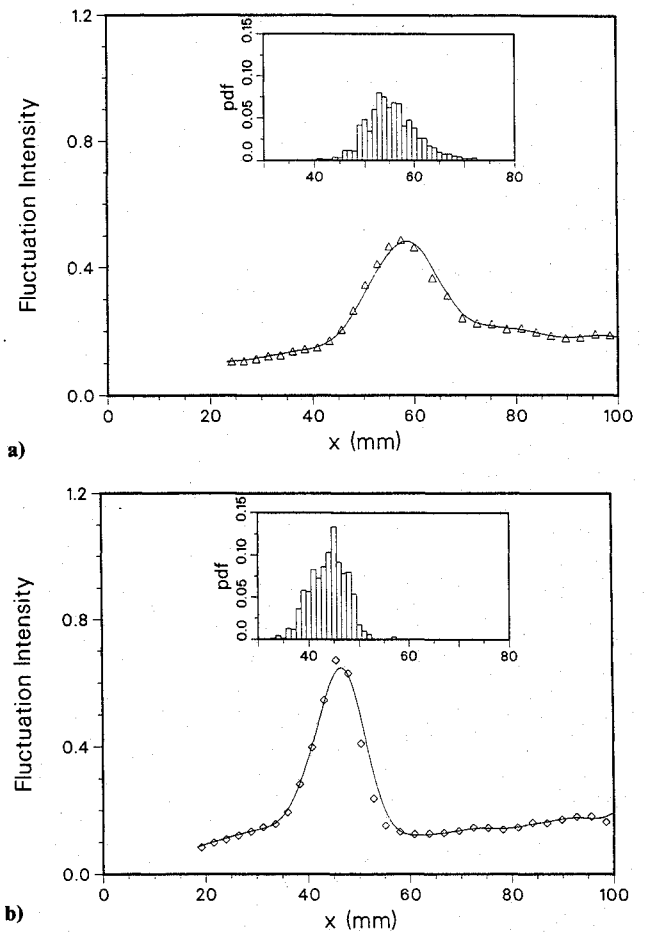

Fig. 7 Pdf of the instantaneous location of centerline CH_4 concentration falloff and centerline rms fluctuations: a) case M; b) case N.

in Fig. 5 are caused by the movement of this boundary. Beyond this boundary, the flow is governed by the airflow and the fluctuations decrease to lower values. The observed behavior of the central jet seen in the images is consistent with the interpretation of velocity data obtained in these flows.[10,24]

Probability density functions (pdf) of the location of the sharp drop in the centerline concentration profiles were obtained to further illustrate the effect of fuel-air jet boundary movement on the rms fluctuations. For these calculations, the location of the sharp drop was selected as the location where the CH_4 concentration crosses a value of 0.2 with a sharp gradient. Figures 7a and 7b show the close correspondence between the sharp-boundary pdfs and the centerline concentration fluctuation profiles for cases M and N, respectively. This correspondence indicates that the large rms fluctuations observed in the stagnation zones of concentric jets are caused by the movement of the large-scale boundary formed between the fuel jet and the recirculating airflow.

These results show that large-scale, time-varying flow features contribute significantly to the turbulent fluctuations in the vicinity of the stagnation points. Since these boundary motions impact fuel/air mixing differently than more classical, small-scale turbulent motion, these features should be treated differently in numerical models of the flow. A conventional time-averaged approach to modeling these features would not be expected to be successful. This was found by Correa,[2] where his time-averaged predictions underpredicted the fluctuations in the vicinity of the stagnation point by nearly a factor of 4. For these essentially large-scale, time-varying structure flows, unsteady turbulent flow models might prove more successful.[25,26]

The length scale associated with the large-scale fluctuations could be obtained from the two-point spatial correlation results. These correlations were calculated from the instantaneous images at selected points in the flow to obtain the domain over which the fluctuations are correlated. The spatial correlation is defined as follows:

$$R_{11}(x,\Delta x,y,\Delta y) = \overline{[c'(x,y)c'(x+\Delta x,y+\Delta y)]}/\overline{[c'(x,y)^2]}^{1/2} \times \overline{[c'(x+\Delta x,y+\Delta y)^2]}^{1/2}$$

where $c'(x,y)$ is the instantaneous CH_4 concentration (with the mean concentration subtracted) at a fixed measurement location (x,y); $\overline{[c'(x,y)^2]}^{1/2}$ is the time-averaged value of the CH_4 fluctuations (x,y); and Δx, Δy represent the spatial distance from the fixed location. The correlations were calculated by assuming a fixed location (x,y) and determining the correlations at variable distances $(x + \Delta x, y + \Delta y)$ from the fixed location from each image. The spatial correlation R_{11} provides a measure of the spatial macroscale of turbulence.

Isocorrelation contour plots for cases L, M, and N are presented in Figs. 8a, 8b, and 8c, respectively. The contour lines shown correspond to values of R_{11} of 0.5 and 0.8. The fixed locations (x,y) are centrally located within the R_{11} contours. The correlations are shown along the centerline ($y = 0$) at $y = 10$ and 20 mm. Correlation contours at radial locations away from the centerline are plotted on alternate sides of the centerline for greater clarity.

For case L (Fig. 8a), which most closely resembles a turbulent jet with no recirculation, length scales along the centerline are initially comparable with the fuel-jet diameter and increase monotonically with downstream distance. The length scales at $y = 10$ and 20 mm are greater than centerline values and reflect the increased structure size adjacent to the central jet. Comparison with Fig. 3a shows that the contours at $y = 10$ mm and at axial distances <50 mm correspond to the recirculation zone established adjacent to the central fuel jet, whereas the region downstream of 50 mm becomes more like a far-field jet with slightly higher velocities near the centerline than in the outer-air flow. The contours at $y = 20$ mm correspond to the outer shear layer, located between the recirculation zone and the annular air. The contours in the shear layer are generally elliptical in shape with the major axis oriented in the axial direction. This indicates that fluid originating from the recirculation zone is being entrained by the higher velocity annular air.

The effect of higher jet-to-air velocity ratios (cases M and N, as shown in Figs. 8b and 8c) on length scales is most apparent along the centerline. Comparison of cases L and M shows that length scales upstream of the case M stagnation zone (located at approximately 60 mm) are comparable. However, in the stagnation region, case M length scales are larger and indicate the presence of large-scale structure in this region. Correlation contours at outer radial locations are comparable for cases L and M, although some increase in stretching of large-scale structures, due to the higher air velocity in case M, is apparent in the outer shear layer.

At the highest air velocity (case N in Fig. 8c), the length scale along the centerline shows two maxima, one at approximately 40 mm and a second at 60 mm downstream. As seen from the velocity measurements in Fig. 3c, both an air- and a fuel-jet stagnation zone exist. The location of these stagnation points coincides closely with the two maxima in length scale, again indicating the importance of large-scale structure in these flows.

Probability distributions of the normalized CH_4 concentration $p(c)$ were calculated from the instantaneous images to help define the relationship between large-scale turbulent structures and time-averaged properties. Shown in Fig. 9a is the centerline variation in $p(c)$ for case L, which is most like a free jet (i.e., no outer-air flow). The distributions along the centerline are typically unimodal and nearly Gaussian at all locations measured. A Gaussian distribution is characteristic

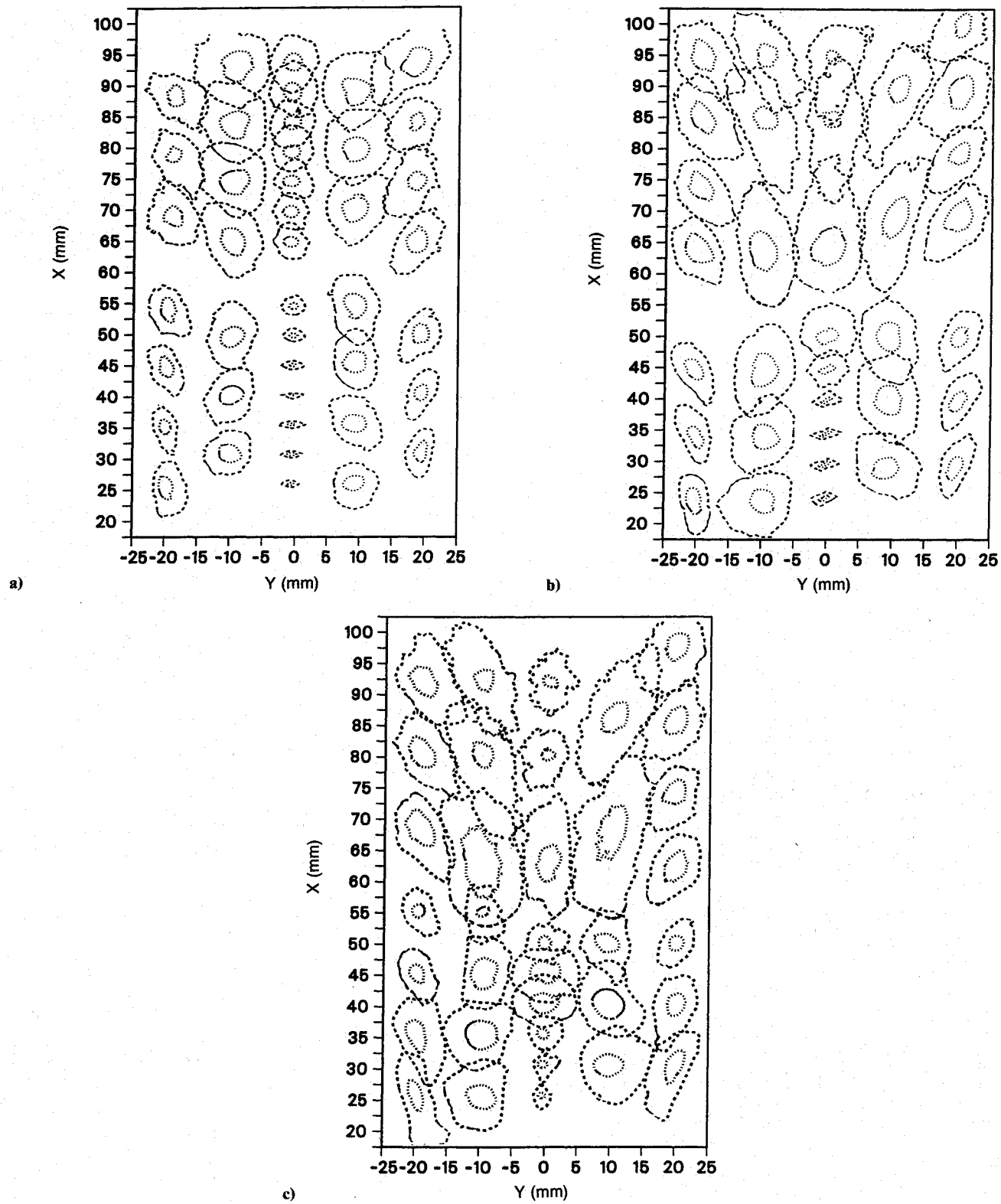

Fig. 8 Isocorrelation contours at selected locations. Contour lines are shown for values of R_{11} = 0.8 (dotted line) and R_{11} = 0.5 (dashed line): a) case L; b) case M; c) case N.

of turbulent fluid that is well mixed at smaller scales and is typical of those found along the centerline of turbulent jets. Nearest the jet exit, at $x \approx 30$ mm, $p(c)$ indicates primarily a mixture of CH_4 and entrained fluid with little unmixed CH_4 remaining. At downstream locations, $p(c)$ shifts to lower values of c with increasing axial distance as additional fluid is entrained by the jet and mixed with jet fluid.

The corresponding centerline variations in $p(c)$ for cases M and N are shown in Figs. 9b and 9c, respectively. At upstream locations ($x \leq 45$ mm for case M and $x \leq 35$ mm for case N), the distributions are qualitatively similar to those of case L, being unimodal and nearly Gaussian. However, farther downstream in the fuel stagnation regions for cases M and N, where fluctuations in the CH_4 concentration are maximum, distributions depart significantly from this Gaussian behavior. This departure is seen as a highly skewed, almost bimodal appearance, in the distributions for case M at axial distances of 50 and 55 mm, and the clearly bimodal distributions in case

N at axial distances of 40 and 45 mm. These locations correspond closely to the respective fuel stagnation points for cases M and N determined from velocity data (see Figs. 3) and further support the fluctuating boundary nature of the flow in the vicinity of the stagnation zone.

Mixing

Figures 10a, 10b, and 10c show radial profiles of the mean and fluctuating rms concentration for cases L, M, and N, respectively. For all three cases, the mean concentration profiles at $x = 20$ mm show a peak corresponding to the central jet and a nearly constant lower concentration region corresponding to the recirculation zone between the central-methane and outer-air jet. The rms fluctuation profiles at $x = 20$ mm show two peaks located at radial locations $y = 4$ and -4 mm in all cases. These peaks correspond to the mixing region adjacent to the central jet. The rms fluctuations in the recirculation zone are lower than at the jet boundary, indicative of a more uniform mixture in this region. This uniformity in recirculation zone concentration is also evident in the instantaneous radial concentration profiles, as illustrated in Fig. 11 for the N case.

In the L case (Fig. 10a) at downstream locations, the constant-concentration recirculation region of the mean profile gradually disappears and, at $x = 80$ mm, the profile becomes similar to the far field of a free jet. For the higher air velocity cases, there is a sharp drop in the concentration profile at around $x = 60$ mm for case M, shown in Fig. 10b, and at around 50 mm for case N, shown in Fig. 10c. These sharp drops correspond to the time-averaged stagnation zones.

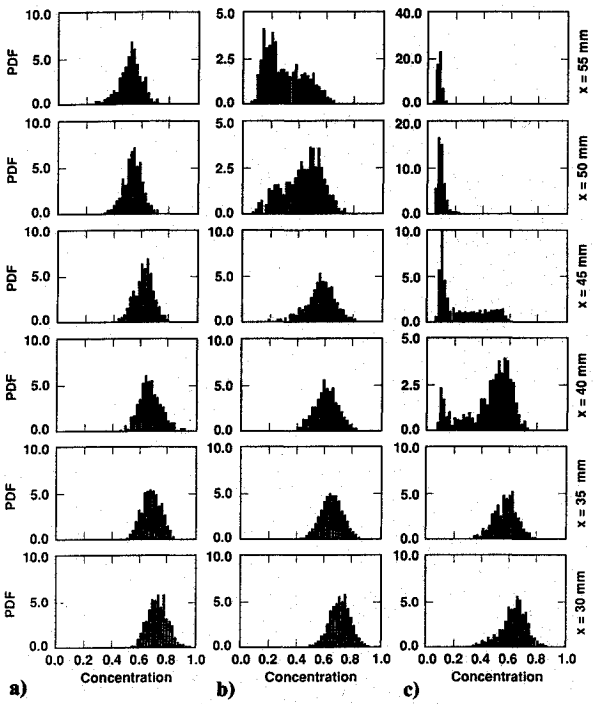

Fig. 9 Centerline CH_4 concentration pdfs: a) case L; b) case M; c) case N.

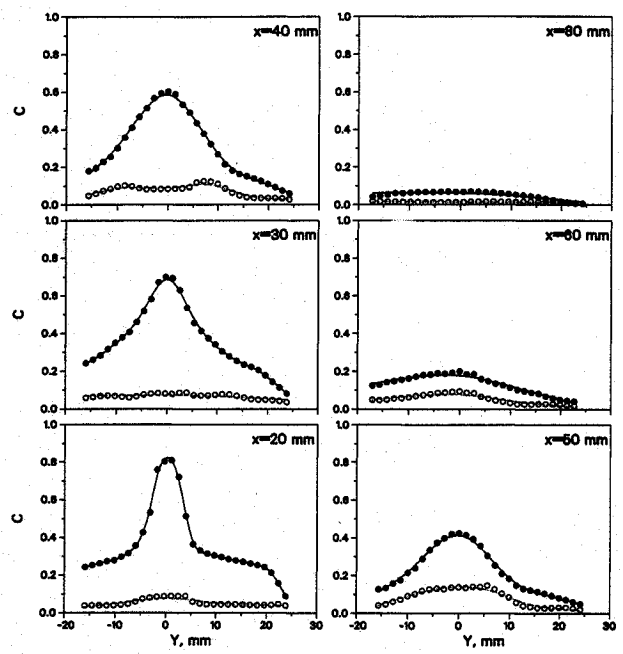

b) Case M

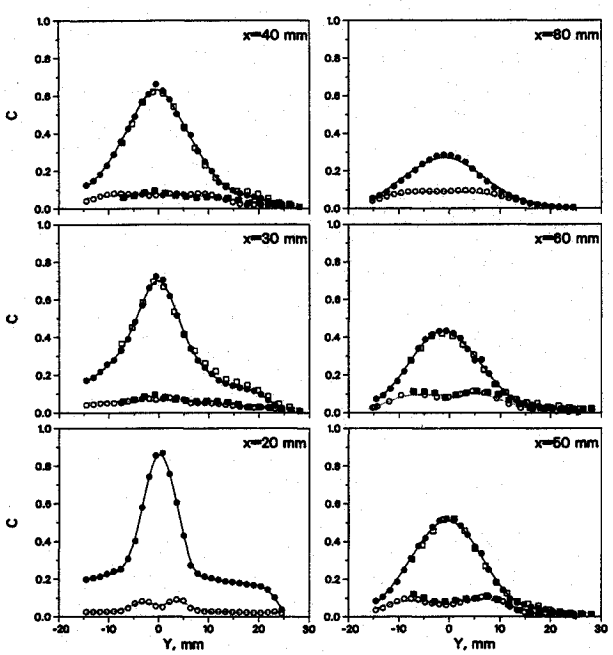

a) ●, ○ case L; ■, □ case P

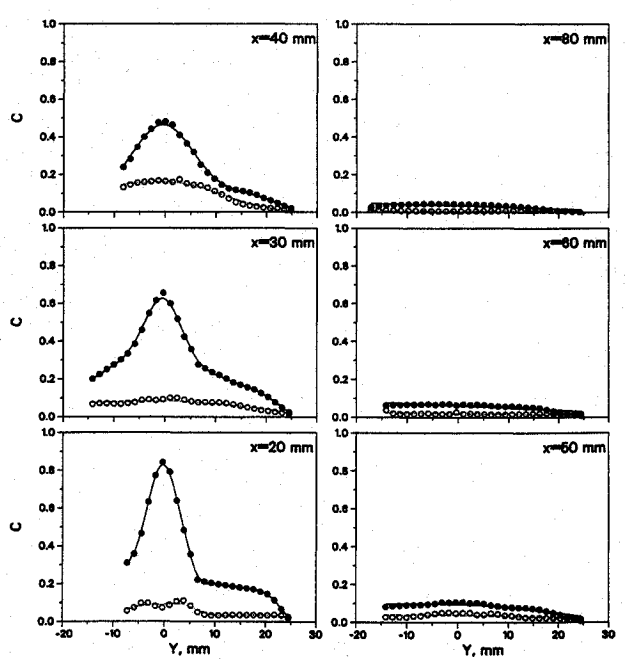

c) Case N

Fig. 10 Radial mean (solid line) and rms fluctuations (dashed line).

Also shown in Fig. 10a are data corresponding to case P of Table 2 with 42-m/s fuel velocity and 15-m/s air velocity, i.e., the same velocity ratio (or momentum-flux ratio) as case L. The data of case P, plotted at x = 30, 40, 50, and 60 mm, closely follow the data of case L, supporting the fact that for similar momentum-flux ratios the mean and rms concentration profiles are the same. Considering the similarity between the concentration fields of cases L and P, these results strongly indicate that for high Reynolds numbers the concentration field is Reynolds number independent and, for a fixed diameter ratio, it is a function of momentum-flux ratio only. The implications of this observation will be discussed in the following section.

What is interesting about these results is that in all cases, particularly the M and N cases, considerable portions of the concentration field have fuel concentrations that lie within the flammability limits of the fuel ($0.05 \leq c \leq 0.15$ for methane). In contrast, for a free jet, only a small portion of the field lies within the flammability limits. This observation is true for both the instantaneous as well as mean results.

Figures 12 show instantaneous contour plots of methane concentration for case D (the free jet) and bluff-body case N. The 0.05, 0.1, and 0.15 fuel concentration contours are given. Note that the 0.05 and 0.15 contours are the approximate lower and upper flammability limits for cold methane-air mixtures and the 0.1 contour corresponds to approximately the stoichiometric mixture condition. In the jet case, shown in Fig. 12a, only a small portion of the field is mixed to a flammable condition where flames can propagate. Therefore, when other conditions for initiating and sustaining flames are met, the flame can only span the region bounded by the lower and upper flammability of the fuel-air mixture. Near the flame initiation point, where reactants are cold, these limits are approximately 0.05 and 0.15, as noted earlier. The confinement of combustion to a narrow zone is consistent with our previous CH/CH_4 results,[20] which showed that the flame spanned a premixed region bounded by the lower and upper flammability limits of the fuel. As shown in Fig. 12b, for the bluff-body case, the region between the 0.05 and 0.15 contour levels occupies a much larger region of the field. This region is where the flame is observed when the mixture is ignited.[17,19,21] Therefore, a key feature of these flows is the ability to rapidly mix fuel and air near the burner to concentration levels suitable for combustion over large portions of the field.

As expected, the area of the field over which flammable concentrations exist is dependent upon the jet-to-air velocity ratio. Figure 13 shows the mean recirculation-zone fuel concentrations at x = 20 and 40 mm and y = 15 mm plotted vs the central jet-to-air velocity ratio. These locations correspond approximately to the locations of the fuel- and the air-driven vortices obtained from the time-averaged velocity field (see Figs. 3), respectively. The velocity ratios corresponding to the N, M, and L cases are indicated on the horizontal axis. Figure 13 also contains the data from the minor test matrix (Table 2) indicated by O, P, M, Q, and R under the horizontal axis. The collapse of these data on one curve shows that, for a given location in the recirculation zone, the fuel concentration is a function of the jet-to-air velocity ratio, or momentum-flux ratio. This observation further indicates that MR is an important similarity parameter. An important observation from these data is that the recirculation zone fuel concentrations have a maximum corresponding to U_j/U_a = 1.4 (MR ≈ 1).

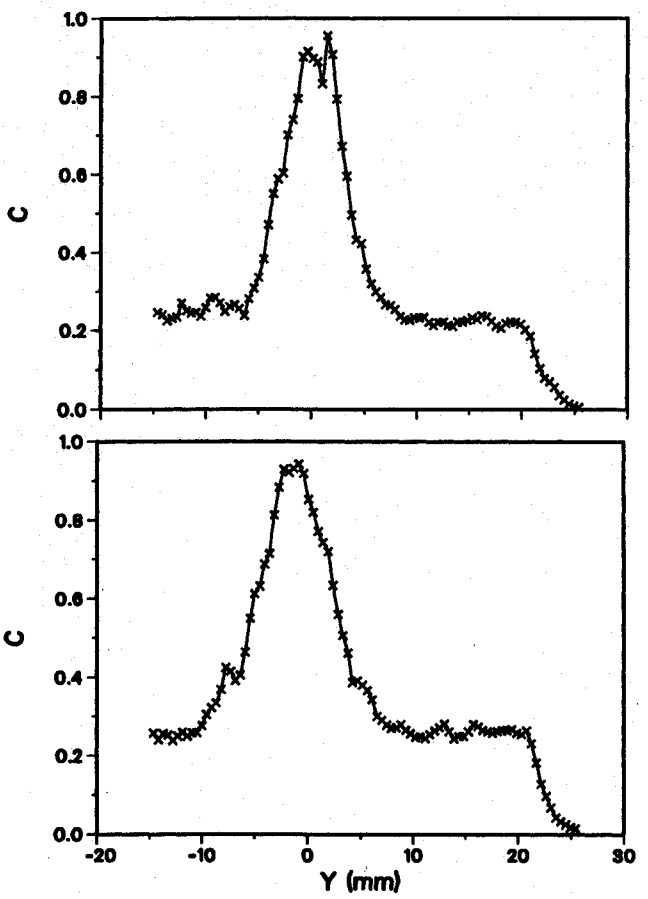

Fig. 11 Instantaneous radial concentration profiles at x = 20 mm for case N.

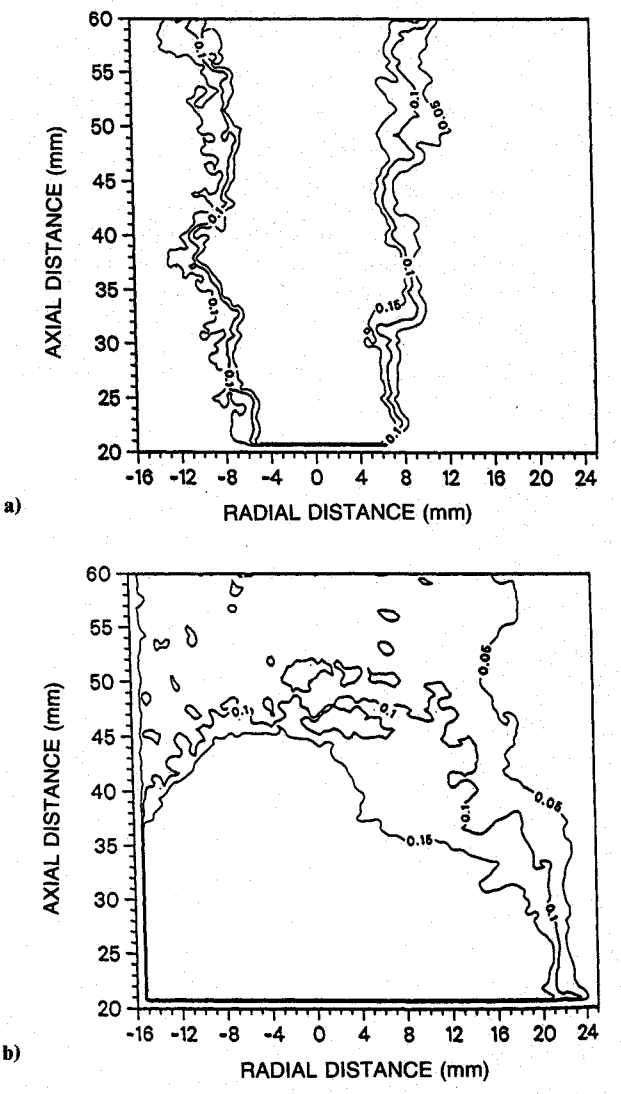

Fig. 12 Flammable region: a) jet; b) bluff body.

This observation can be explained by noting that for a fixed air velocity, as the fuel velocity increases from zero, the fuel jet is stagnated and dispersed into the recirculation zone and the fuel concentration increases. The maximum fuel concentration in the recirculation zone is achieved just before the fuel jet penetrates the recirculation zone (MR ≈ 1). At higher fuel-jet velocities, the fuel jet penetrates through the recirculation zone. As the fuel velocity continues to increase, more of the fuel jet is able to penetrate the recirculation zone and the fuel concentration decreases. What is most significant about the results in Fig. 13 is that the fuel- and air-vortex concentrations are within the flammability limits only for selected velocity ratios and that these limits are exceeded at different velocity ratios. Therefore, flames can either be detached from the burner (stabilized in the downstream air vortex) or attached (stabilized in the upstream fuel vortex) depending on which velocity ratio is selected. This behavior has been observed experimentally.[21,27]

As indicated earlier, when the fuel jet is stagnated, there is a large increase in fuel/air dispersion and mixing. It is expected that the presence of recirculation will enhance mixing even for the penetrated cases. To evaluate the increase in mixing, the radial concentration profiles were normalized and compared with free-jet results. Figure 14 shows the mean radial profiles of Fig. 10a (case L) plotted in nondimensional form. The radial locations are nondimensionalized by the half radius of a free jet, $Y_{1/2}$.[28] The nondimensionalized concentration is defined as $(C - C_0)/(C_{cl} - C_0)$, where C_{cl} is the centerline concentration and C_0 is the concentration at $2Y_{1/2}$. Velocity data for case L (Fig. 3a) show that the recirculation zone extends to an axial distance of about 50 mm. The data of Fig. 14 thus represent measurements both within and outside (downstream) of the recirculation zone. As shown in Fig. 14, the central-fuel-jet data ($y/Y_{1/2} \leq 2$) downstream of the recirculation zone at $x = 60$ and 80 mm are consistent with the free-jet profile (solid line). Concentration profiles upstream of this location show increased spreading relative to the free jet, indicating that jet mixing is enhanced by the presence of the recirculation zone. Downstream of the recirculation zone, the flow behaves like a free jet, but with a lower centerline concentration (see Figs. 3, case L). Similar analyses performed for the M and N cases show even more substantial enhancement of mixing by the recirculation zone at the higher air velocities. These results illustrate the major impact of the recirculation zone on jet mixing.

Discussion

In this paper, we presented the first concentration-imaging data in concentric jets, also known as bluff-body flows. For the nonreacting data presented, the data represent a conserved scalar. The imaging system used revealed large-scale aspects of the flow and allowed interpretation of the mean and rms fluctuating concentration results in that context. Length scales associated with these fluctuations were obtained. It was demonstrated that the large concentration fluctuations in stagnation regions were the result of large-scale movement in the fuel-air boundary near the stagnation point. This observation points to the limitation of time-averaged k-ε models[2,3] in predicting these fluctuations. Data presented elsewhere[19,20] show that flames form in the stagnation region along fuel/air boundaries, thus indicating that modeling of these fluctuations is essential to correct combustion models. Higher order models, or large eddy simulation models,[25,26] capable of including intermittency effects may be needed to adequately predict these flows. The data presented in this paper should be useful for the development and validation of these models.

Although the present flows are governed by large-scale structure, it was shown in Figs. 10 and 13 that a similarity exists between the mean and rms concentration fields. In Figs. 10, radial profiles of the mean and rms concentration at the same velocity ratio were shown to be similar over a factor of 2 change in Reynolds number. In Fig. 13, it was shown that, at a given point, the mean concentration for all of the cases of Tables 1 and 2 collapse onto a single curve. Similar results for the mean and rms values not presented in the paper were obtained at other points in the recirculation zone. Therefore, these results strongly indicate that the mean and rms concentration field scales with the velocity ratio.

The authors realize the limitations of the present data in making a strong conclusion about the similarity of concentration fields over a large range of momentum-flux ratios. The present data do not test the effect of density ratio, and a more stringent test of the similarity seen in Fig. 10a is performed at only one velocity ratio ($U_j/U_a = 2.8$). Figure 13 data only support the similarity up to velocity ratios of 2.8 (MR = 4.3). Beyond this velocity ratio, sufficient data points are not available to extend the conclusion. However, these data should be viewed in the context of previously reported similarity of other parameters such as stagnation point location, flame shape, flame regimes, etc.

Scaling of the stagnation point location with $MR = \rho_j U_j^2/\rho_a U_a^2$ has been demonstrated by several authors.[15,27] Kelly et al.[27] derived this parameter by balancing the dynamic pressure of the central jet and concentric air on the axis and were able to correlate central-jet penetration data in bluff-body flows. Li and Tankin[15] used an elaborate analysis to correlate jet penetration length with jet and air Reynolds numbers and with jet, bluff-body, and air diameter ratios, When the correlation is simplified, it shows that the jet penetration, i.e., location of fuel-jet stagnation point, is only a function of $MR^{1/2}$ and d_j/d_b (d_j is the central jet diameter and d_b is the bluff-

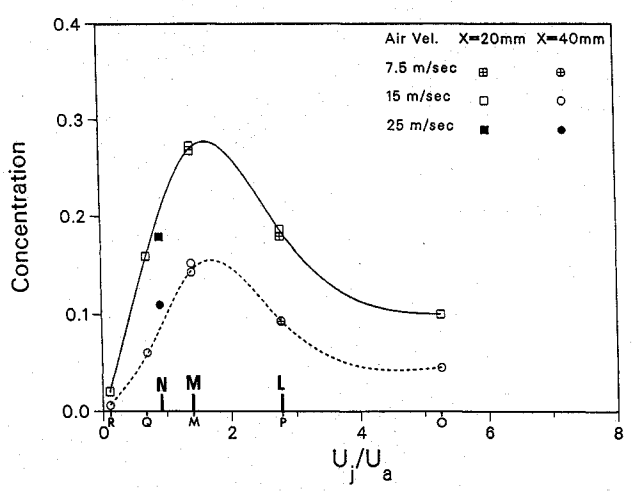

Fig. 13 Recirculation zone mean concentration profiles as a function of jet-to-air velocity ratio at y = 15 mm.

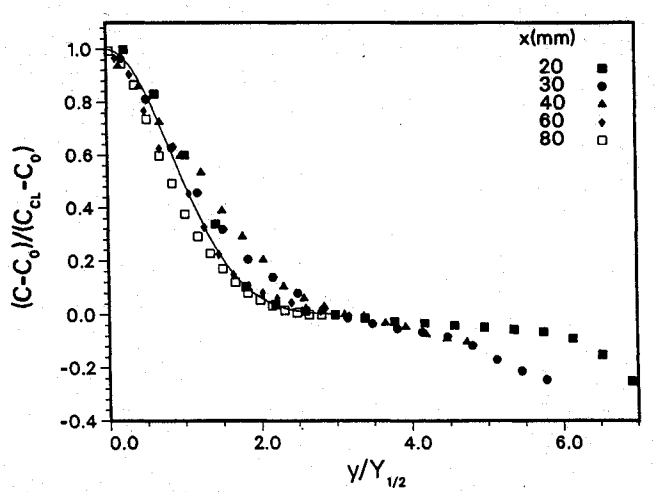

Fig. 14 Normalized mean radial concentration profiles for case L.

body diameter). With this derivation, Li and Tankin[15] were able to correlate jet penetration data from several studies, including data from the present authors.[17] Considering that the jet penetration is very important in defining the flowfield, it is reasonable to assume that MR and diameter ratio are important scaling parameters.

The present bluff-body produces different types of flames.[21,27] At $U_j/U_a < 0.2$, no flame exists (lower blowout limit). At $0.2 < U_j/U_a < 0.6$, the flame is attached to the bluff body. As U_j/U_a is increased, the flame detaches from the bluff body (at $U_j/U_a \approx 0.6$). Further increasing the velocity ratio, the flame reattaches (at $U_j/U_a \approx 3$). These observations were made for $0 \leq U_j \leq 100$ and $0 \leq U_a \leq 30$ m/s.[21,27] The fact that regardless of the air or the fuel velocity the flame type depends only on the velocity ratio also supports the similarity argument.

Further evidence that momentum-flux ratio is a universal similarity parameter for bluff-body flows comes from the scaling analysis presented by Chen et al.,[29] which allowed a comparison of data from a swirl-stabilized flame to data obtained in the present bluff-body flow. In the cited work, the flow was considered as a central jet with momentum $\rho_j U_j^2 d_j^2$, interacting with an air-driven vortex with circulation Γ. The circulation strength is defined as

$$\Gamma = U_{rz} \cdot b$$

where U_{rz} is an average reverse-flow velocity created by the air recirculation zone and b is the radius of the recirculating vortex. Two nondimensionalized parameters were then defined as

$$\Gamma^* = \rho_a^{1/2} \Gamma / \rho_j^{1/2} U_j d_j$$

$$\mathrm{MR} = \rho_j U_j^2 / \rho_a U_a^2$$

which are the normalized vortex-induced momentum Γ^* and the normalized jet momentum, or jet-to-air momentum-flux ratio MR. It was shown that if these two parameters were the same, swirl and bluff-body burners create similar flames, thus indicating that MR and Γ^* are similarity parameters for these two different burners.

Using d_b as the bluff-body diameter, the relation between these two parameters can be rearranged as

$$\Gamma^* = \mathrm{MR}^{-1/2}(d_b/d_j)(U_{rz}/U_a)(b/d_b)$$

Table 3 shows the experimental values for the last two terms in this equation. As shown, the values are the same for all MRs studied. Therefore, in the present noncombusting bluff-body flow, the following relation holds:

$$\Gamma^* = 0.044(\mathrm{MR})^{-1/2}(d_b/d_j)$$

This relation is used to calculate the Γ^* values in Table 3. As seen from this relation, the momentum-flux ratio and the ratio of jet to bluff-body diameter are the only similarity parameters for the present bluff-body flows.

Chen et al.[29] suggests that Γ^* is a universal parameter for recirculating flows such as the present bluff-body flows. However, it is a parameter that is difficult to determine because it requires the measurement of velocity over the entire field to define U_{rz} and b. As shown by the previous relation, MR and d_b/d_j define Γ^* in the present bluff-body flows. For this reason, MR and d_b/d_j have been emphasized as similarity parameters in this paper. It is important to note, however, that other bluff-body parameters can change Γ^*. As an example, the use of a conical bluff body[30] or the presence of confinement walls in the immediate vicinity of the bluff body[31] will change the recirculation-zone flow pattern and size and, therefore, Γ^*. MR should, therefore, be considered a similarity parameter for a fixed geometry only.

Table 3 Recirculation-zone parameters

MR	u_{rz}/u_a	b/d_a	Γ^*	Case
4.32	0.20	0.22	0.85	L
1.08	0.20	0.22	0.42	M
0.389	0.19	0.23	0.25	N

Summary

Planar CH_4 concentration imaging results are reported for a concentric jet of CH_4 fuel and air separated by a bluff body. Several jet-to-air velocity ratios were studied under isothermal conditions. The jet-to-air velocity ratio, or momentum-flux ratio, is an important parameter in fuel and air mixing. When the momentum-flux ratio is <1, the jet penetrates the recirculation zone formed behind the bluff body. At momentum-flux ratios >1, the fuel jet is stagnated and does not penetrate the recirculation zone and fuel is dispersed into the recirculation zone.

For a given bluff-body-to-jet-diameter ratio, limited results are presented that indicate that the mean and fluctuating concentration profiles are the same for the same momentum-flux ratio. These results, when considered with other data and analyses presented in the literature, indicate that the momentum-flux ratio may be a scaling parameter for bluff-body flows. Further measurements over a wider range of momentum-flux ratios are needed to verify this conclusion.

Flow and mixing for nonpenetrated cases are dominated by larger-scale, time-varying fluctuations of fuel/air boundaries near the stagnation zone. Since flames form in these zones along the fuel/air boundaries, adequate predictions of these fluctuations may be required to model combusting flows. These fluctuations are not adequately predicted by current time-averaged models. It is therefore likely that time-dependent approaches will be needed to accurately predict fluctuations in the stagnation region and, thereby, the combustion characteristics of these flows.

The momentum-flux ratio also governs the fuel concentration inside the recirculation zone. For low momentum-flux ratios, considerable portions of the field are mixed to conditions where combustion could occur. These regions occupy a much greater portion of the field than those for free-jet flames with no bluff body present. This enhanced mixing is the reason for more stable flames in these burners. Penetrated-jet cases show increased mixing relative to a free jet inside the recirculation zone, whereas downstream of the recirculation zone the flow is similar to a free jet.

Acknowledgments

This work was supported by the Physical Sciences Department, Gas Research Institute, through Altex Technologies Corporation and by the U.S. Department of Energy, Office of Basic Energy Sciences, Division of Chemical Sciences, through Sandia National Laboratories at Livermore, California.

References

[1]Beer, J. M., and Chigier, N. A., *Combustion Aerodynamics*, Krieger, Malabar, FL, 1983.

[2]Correa, S. M., "Prediction of an Axisymetric Combusting Flow," *AIAA Journal*, Vol. 22, No. 11, 1983, pp. 1602–1608.

[3]Krishnamurthy, L., Park, S. O., Wahrer, D. J., and Cochran, H. S., "Laser Diagnostic Development and Measurement and Modeling of Turbulent Flowfields of Jets and Wakes, Part II: Numerical Predictions of Isothermal Flowfields in a Ducted Centerbody Combustor," Air Force Wright Aeronautical Lab., AFWAL-TR-83-2044, Wright-Patterson AFB, OH, June 1983.

[4]Sturgess, G. J., and Syed, S. A., "Widely-Spaced Co-Axial Jet, Diffusion-Flame Combustor: Isothermal Flow Calculations Using the Two-Equation Turbulence Model," AIAA Paper 82-0113, Jan. 1982.

[5]Durao, D. F. G., and Whitelaw, J. H., "Velocity Characteristics of Disk-Stabilized Diffusion and Premixed Flames," *Experimental Diagnostics in Gas Phase Combustion Systems*, edited by B. T. Zinn, Vol. 53, Progress in Astronautics and Aeronautics, AIAA, New York, 1977, pp. 395–409.

[6]Calvert, J. R., "Experiments on Low-Speed Flow Past Cones," *Journal of Fluid Mechanics*, Vol. 27, Pt. 2, 1967, pp. 273–289.

[7]Lightman, A. J., Richmond, R. D., and Krishnamurthy, L., "Velocity Measurements in a Bluff-Body Diffusion Flame," AIAA Paper 80-1544, AIAA 15th Thermophysics Conf., Snowmass, CO, July 1980.

[8]Samuelsen, G. S., "Mechanisms of Exhaust Pollutants and Plume Formation in Continuous Combustion," Univ. of California, Irvine, CA, AFOSR Rept. UCI-ARTR-84-7, June 1984.

[9]Roquemore, W. M., Bradley, R. P., Stutrud, J. S., Reeves, C. M., Obringer, C. A., and Britton, R. L., "Utilization of Laser Diagnostics to Evaluate Combustor Models," AGARD-CP-353, 1983, pp. 36-1–36-21.

[10]Schefer, R. W., Namazian, M., and Kelly, J., "Velocity Measurements in a Turbulent Nonpremixed Bluff-Body Stabilized Flame," *Combustion Science and Technology*, Vol. 56, 1987, pp. 101–138.

[11]Kimoto, K., Shiraishi, I., and Matsumoto, R., "Structure of Turbulent Jet Flames Stabilized in Annular Air Jet," *Combustion Science and Technology*, Vol. 25, 1981, pp. 31–41.

[12]Roquemore, W. M., Bradley, R. P., Stutrud, J. S., Reeves, C. M., and Krishnamurthy, L., "Preliminary Evaluation of a Combustor for use in Modeling and Diagnostics Development," American Society of Mechanical Engineers, New York, ASME 80-GT-93, 1980.

[13]Lightman, A. J., and Magill, P. D., "Velocity Measurements in Confined Dual Coaxial Jets Behind an Axisymmetric Bluff Body: Isothermal and Combusting Flows," Air Force Wright Aeronautical Lab., AFWAL-TR-81-2016, Wright-Patterson AFB, OH, April 1981.

[14]Roquemore, W. M., Tankin, R. S., Chiu, H. H., and Lottes, A. A., "The Role of Vortex Shedding in a Bluff-Body Combustor," *Experimental Measurement and Techniques in Turbulent Reactive and Nonreactive Flows*, edited by J. H. Whitelaw and M. Lapp, AMD, Vol. 66, American Society of Mechanical Engineers, New York, 1984.

[15]Li, X., and Tankin, R. S., "A Study of Cold and Combusting Flow Around Bluff-Body Combustors," *Combustion Science and Technology*, Vol. 52, 1987, pp. 173–206.

[16]Roquemore, W. M., Tankin, R. S., Chiu, H. H., and Lottes, A. A., "A Study of a Bluff-Body Combustor Using Laser Sheet Lighting," *Experiments in Fluids*, Vol. 4, 1986, pp. 205–213.

[17]Namazian, M., Kelly, J. T., and Schefer, R. W., "Flow and Combustion in Bluff-Body Stabilized Flames," The Combustion Institute, Paper 2-1B, Pittsburgh, PA, 1985.

[18]Schefer, R. W., Namazian, M., and Kelly, J., "Comparison of Turbulent-Jet and Bluff-Body Stabilized Flames," *Combustion Science and Technology*, Vol. 67, 1989, pp. 123–146.

[19]Namazian, M., Kelly, J., Schefer, R. W., Johnston, S. C., and Long, M. B., "Nonpremixed Bluff-Body Burner Flow and Flame Imaging Study," *Experiments in Fluids*, Vol. 8, 1989, pp. 216–228.

[20]Namazian, M., Kelly, J., and Schefer, R. W., "Near-Field Instantaneous Flame and Fuel Concentration Structure," *Twenty-Second (International) Symposium on Combustion*, 1988, pp. 627–634.

[21]Kelly, J. T., Namazian, M., Schefer, R. W., and Perrin, M., "Characterization of Nonpremixed Bluff-Body Stabilized Flames," 1988 Gas Research Institute Annual Rept., GRI 89/0105, 1989.

[22]Namazian, M., Schefer, R. W., and Kelly, J., "Scalar Dissipation Measurements in the Developing Region of a Jet," *Combustion and Flame*, Vol. 74, 1988, pp. 147–160.

[23]Long, M. B., Fourguette, D. C., Escoda, M. C., and Layne, C. B., "Instantaneous Ramanography of a Turbulent Diffusion Flame," *Optics Letters*, Vol. 9, 1983, pp. 244–246.

[24]Kelly, J. T., Namazian, M., Schefer, R. W., and Perrin, M., "Characterization of Nonpremixed Bluff-Body Stabilized Flames," 1987 GRI Annual Rept., GRI 88/0168, 1988.

[25]Ghoniem, A. F., Chorin, A. J., and Oppenheim, A. K., "Numerical Modeling of Turbulent Flow in a Combustion Tunnel," *Philosophical Transactions of the Royal Society of London, Series A: Mathematical and Physical Sciences*, Vol. 304, 1982, pp. 303–315.

[26]Orszag, S. A., "Spectral Methods for Problems in Complex Geometries," *Journal of Computational Physics*, Vol. 37, 1980, pp. 70–92.

[27]Kelly, J., Namazian, M., and Schefer, R. W., "Bluff-Body Burner Flows, Fuel Concentrations and Flame Regimes," American Society of Mechanical Engineers Conf., Houston, TX, Jan. 1989.

[28]Pitts, W. M., and Kashiwagi, T., "The Application of Laser-Induced Rayleigh Light Scattering to the Study of Turbulent Mixing," *Journal of Fluid Mechanics*, Vol. 141, 1984, pp. 391–429.

[29]Chen, R., Driscoll, J. F., Kelly, J., Namazian, M., and Schefer, R. W., "A Comparison of Bluff-Body and Swirl-Stabilized Flames," *Combustion Science and Technology*, Vol. 71, 1990, pp. 197–217.

[30]Taylor, M. K. P., and Whitelaw, J. H., "Velocity Characteristics in the Turbulent Near Wakes of Confined Axisymmetric Bluff-Bodies," *Journal of Fluid Mechanics*, Vol. 139, 1984, pp. 391–416.

[31]Perrin, M., Namazian, M., Kelly, J., and Schefer, R. W., "Effect of Confinement and Blockage Ratio on Nonpremixed Turbulent Bluff-Body Burner Flames," Twenty-Third (International) Symposium on Combustion, Poster 173, Orleans, France, July 1990.